A 26-GHz GaN MMIC Load-Modulated Balanced Amplifier With Miniaturized Dual-Loop Coupler

Haoyang Jia, *Graduate Student Member, IEEE*, Ruijia Liu, *Member, IEEE*, Qian Wu, *Graduate Student Member, IEEE*, and Anding Zhu, *Fellow, IEEE*

***Abstract*— This article presents the analysis and design of a 26-GHz RF-input load-modulated balanced amplifier (LMBA) using a miniaturized dual-loop (MDL) coupler, implemented in a 0.12-μm gallium nitride (GaN) high-electron-mobility transistors (HEMTs) process. The MDL coupler is proposed to reduce the chip area while ensuring good isolation without compromising the load modulation of the LMBA. The design space of the coupler is expanded by employing dual-loop coupled lines with shunt and coupling capacitors. The miniaturized coupler facilitates the implementation of millimeter-wave LMBA in monolithic microwave-integrated circuits (MMICs). To validate the design, a GaN MMIC LMBA incorporating the proposed MDL coupler is designed and implemented. The fabricated LMBA can deliver more than 36.35-dBm saturated power at 26 GHz with a drain efficiency (DE) of 35.06% at peak and 24.5% at 6-dB power back-off (PBO). When driven by a 100-MHz fifth-generation (5G) new radio (NR) frequency range 2 (FR2) 64-QAM signal, the proposed LMBA achieves an average output power of 28 dBm, an adjacent channel leakage ratio (ACLR) better than −47 dBc, and an error vector magnitude (EVM) of −34.11 dB after digital predistortion.**

***Index Terms*— Coupler, gallium nitride (GaN), high efficiency, high power, load-modulated balanced amplifier (LMBA), monolithic microwave-integrated circuits (MMICs), power back-off (PBO).**

I. Introduction

EMERGING technologies are being developed to improve wireless throughput in the fifth-generation (5G) mobile network. The surge in demand for high data rates, spectrum-efficient modulation schemes with high peak-to-average power ratio (PAPR) signals are increasingly deployed in wireless communication systems. This poses stringent linearity and efficiency requirements on RF power amplifiers (PAs), particularly on power back-off (PBO) efficiency.

Extensive research has been carried out in developing advanced PA architectures for better PBO performance, such as Doherty PA (DPA), enveloping tracking, and outphasing amplifiers. Among them, DPA is the most widely used PA architecture, particularly in high-power applications [1], [2], [3], [4], [5], [6], [7], [8], [9], [10], [11], [12], [13]. However, designing high-efficiency DPAs at millimeter-wave frequencies becomes increasingly challenging due to high losses in passive components, such as transmission line-based load modulation networks.

In [14], a new PA architecture called load-modulated balanced amplifier (LMBA) is proposed, where a control signal is injected into the balanced amplifier (BA) via the isolated port of a coupler. It leverages the control signal amplifier (CA) to modulate the output impedance of BA for excellent efficiency enhancement. Recently, various LMBA architectures have been developed to improve PBO efficiency and bandwidth (BW) performance, but the couplers in LMBA are rarely investigated [14], [15], [16], [17], [18], [19], [20], [21], [22]. In LMBA, the coupler is one of the most critical components, because it directly affects the BW, output power, efficiency, and even dominates the chip area. It is particularly challenging to implement a compact coupler with minimal insertion loss, especially in the monolithic microwave-integrated circuit (MMIC) [23]. In addition, the performance of the coupler in terms of the isolation and magnitude/phase error also significantly affects the load modulation operation in LMBA. Therefore, it is worth putting more efforts into the coupler design for LMBA.

Among the reported LMBAs, the most commonly used coupler structure is the branch-line coupler, which leverages $\lambda/4$ TLs as four arms to formulate the coupler. The branch-line coupler can provide excellent directivity, which is a superior advantage to maintaining effective load modulation compared with other typologies. However, the single-stage branch-line coupler has a limited BW, and thus, multistage branch-line couplers are usually cascaded to expand the BW [20]. As a result, the penalty is paid for the increased footprint of the coupler.

Lange coupler is another frequently used structure in LMBA [24], [25], [26]. It employs several parallel lines coupled with each other in a fringing field at both edges. Using this structure, the coupler can easily achieve a 3-dB coupling ratio with a wide BW. However, it is often difficult to implement tightly coupled lines in MMIC, because the space between parallel lines is limited by the physical rules of fabrication process. Recently, a monolithic-integrated coupler is proposed in [27], where two coupled inductors are used to achieve a 3-dB coupling ratio with broadband performance. Nevertheless, it is hard to implement in mm-wave circuits,

Manuscript received 11 April 2024; revised 2 June 2024 and 24 June 2024; accepted 27 June 2024. This work was supported in part by the Science Foundation Ireland under Grant 13/RC/2077_P2. *(Corresponding author: Haoyang Jia.)*

The authors are with the School of Electrical and Electronic Engineering, University College Dublin, Dublin 4, D04 V1W8 Ireland (e-mail: haoyang.jia@ucdconnect.ie; ruijia.liu@ucd.ie; qian.wu@ucdconnect.ie; anding.zhu@ucd.ie).

Color versions of one or more figures in this article are available at https://doi.org/10.1109/TMTT.2024.3421941.

Digital Object Identifier 10.1109/TMTT.2024.3421941

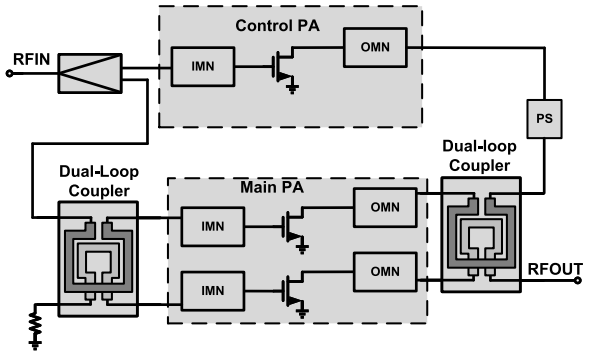

Fig. 1. Simplified block diagram of the proposed LMBA with MDL couplers.

because the coupling coefficient between inductors is difficult to realize with the increase of frequency due to the existence of the self-resonant frequency (SRF).

In this article, we propose a miniaturized dual-loop (MDL) coupler structure to reduce chip size and improve isolation, which facilitates MMIC implementation. To validate the design, a 26-GHz gallium nitride (GaN) MMIC LMBA using the proposed MDL coupler is designed and implemented in a 0.12-μm GaN high-electron-mobility transistor (HEMT) process, as shown in Fig. 1. To the best of our knowledge, this is the smallest coupler with a size of 265 $\times$ 240 μm^2 implemented in GaN MMIC. To achieve the targeted PBO level, an uneven power divider is used to generate the required power dividing ratio. The fabricated LMBA can deliver more than 36.35-dBm saturated power at 26 GHz with a drain efficiency (DE) of 35.06% at peak and 24.5% at 6-dB PBO. When driven by a 100-MHz 5G new radio (NR) frequency range 2 (FR2) 64-QAM signal, the proposed LMBA achieves an average output power of 28 dBm, an adjacent channel leakage ratio (ACLR) better than -47 dBc, and an error vector magnitude (EVM) of -34.11 dB after digital predistortion.

The remaining part of this article is organized as follows. In Section II, the operating principle of the proposed MDL coupler is presented. Section III shows the implementation of the designed RF-input LMBA using the proposed MDL couplers. The measurement results are shown in Section IV. Finally, the conclusion is given in Section V.

II. Proposed MDL Coupler

A. Theoretical Analysis

Fig. 2 shows the structure of the traditional coupled-line coupler where the electric length of the coupled lines is designed to be $\lambda/4$ to achieve the operation of the ideal 3-dB codirectional coupler. This structure unfortunately occupies a large chip area in MMIC process. To address this challenge, we propose a dual-loop coupler, shown in Fig. 3, which consists of two coupled-line sections with an electrical length of θ and even-/odd-mode characteristic impedance of Z_{0e} and Z_{0o}, and two capacitors C_1 at the middle of TL with the electrical length θ_0 and characteristic impedance Z_0. By introducing shunt capacitors C_1, the flexibility of coupler design is increased, which allows the utilization of coupled lines of shorter electrical lengths and, thus, reduces the chip area in MMIC.

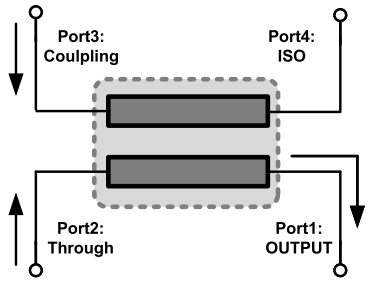

Fig. 2. Schematic of the traditional coupled-line coupler.

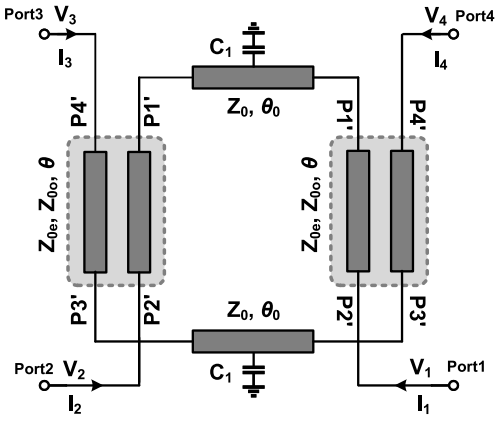

Fig. 3. Schematic of the proposed MDL coupler.

To intuitively understand the behavior of this structure, we analyze the proposed MDL coupler by using the even-/odd-mode analysis [28]. At first, we derive the even-mode scattering parameters of the half circuit under even-mode excitation by converting the four-port network of the ideal coupled line into a two-port network. Then, the odd-mode scattering parameters can also be obtained with the odd-mode excitation similarly. Thus, using the even-/odd-mode scattering parameters, the $[S]$ matrix of the proposed MDL coupler is obtained, and the relative variable relationships can also be derived with the boundary conditions.

If we apply the even-mode signal to Ports 1 and 2, shown in Fig. 3, the intermediate node of TL will be virtual open, and the capacitors $C_1/2$ are directly connected to half of the TL, as shown in Fig. 4(a). In the odd-mode excitation, the intermediate node of TL behaves like the virtual ground, and then, TL acts as an inductor with electrical length $\theta_0/2$ connected to the coupled lines, as shown in Fig. 4(b). The ideal coupled-line section with four ports (P1′, P2′, P3′, and P4′) can be characterized by its $[S]$ matrix given by [29], [30]

$$[S] = \begin{bmatrix} 0 & \frac{\sqrt{1-k^2}}{\Phi} & \frac{jk\sin\theta}{\Phi} & 0 \\ \frac{\sqrt{1-k^2}}{\Phi} & 0 & 0 & \frac{jk\sin\theta}{\Phi} \\ \frac{jk\sin\theta}{\Phi} & 0 & 0 & \frac{\sqrt{1-k^2}}{\Phi} \\ 0 & \frac{jk\sin\theta}{\Phi} & \frac{\sqrt{1-k^2}}{\Phi} & 0 \end{bmatrix} \quad (1)$$

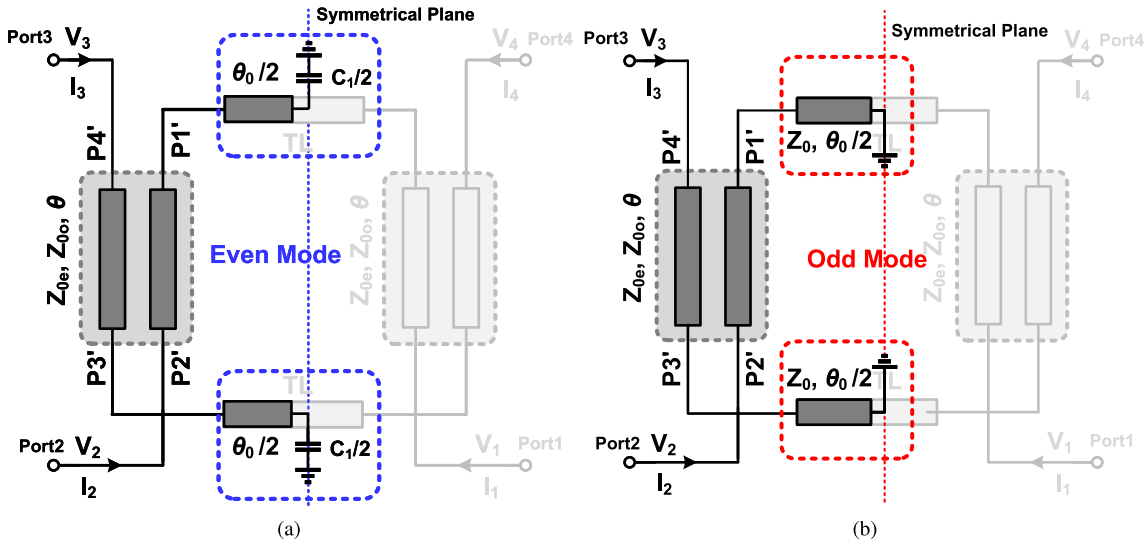

Fig. 4. Equivalent schematic of the proposed coupler. (a) Even mode. (b) Odd mode.

where

$$k = \frac{Z_{0e} - Z_{0o}}{Z_{0e} + Z_{0o}} \tag{2}$$

$$\Phi = \sqrt{1-k^2}\cos\theta + j\sin\theta \tag{3}$$

$$Z_0 = \sqrt{Z_{0o}Z_{0e}}. \tag{4}$$

Z_0 is the characteristic impedance of the coupled lines. Note that the characteristic impedance of all the TLs in this analysis is assumed to be Z_0 to ease the mathematical derivation. The operation of the proposed coupler in the even-mode excitation can be described by the $[S]$ matrix

$$\begin{bmatrix} b_1 \\ b_2 \\ b_3 \\ b_4 \end{bmatrix} = [S_e] \begin{bmatrix} a_1 \\ a_2 \\ a_3 \\ a_4 \end{bmatrix} \tag{5}$$

where a_n is the amplitude of the voltage wave incident on port N and b_n is the amplitude of the voltage wave reflected from port N. As shown in Fig. 4(a), the capacitors $C_1/2$ and TLs $\theta_0/2$ are connected to P1′ and P3′, so the following equations are given:

$$\Gamma_e = \frac{(2 - (j\tan(\theta_0/2)))(j\omega C_1 Z_{0e} - 1)}{(j\tan(\theta_0/2) + 1)(j\omega C_1 Z_{0e} + 2)} \tag{6}$$

$$a_1 = \Gamma_e b_1 \tag{7}$$

$$a_3 = \Gamma_e b_3 \tag{8}$$

where Γ_e represents the reflection coefficient of P1′ and P3′ in even mode. By introducing (6)–(8) into (5), the four-port network can be simplified to a two-port network as follows:

$$\begin{bmatrix} b_2 \\ b_4 \end{bmatrix} = \begin{bmatrix} S_{22,e} & S_{24,e} \\ S_{42,e} & S_{44,e} \end{bmatrix} \times \begin{bmatrix} a_2 \\ a_4 \end{bmatrix} \tag{9}$$

where

$$S_{22,e} = S_{44,e} = \frac{\left(1 - k^2 - k^2(\sin\theta)^2\right)\Gamma_e}{\Phi^2} \tag{10}$$

$$S_{24,e} = S_{42,e} = \frac{\left(jk\sqrt{1-k^2}\sin\theta\right)\Gamma_e}{\Phi^2}. \tag{11}$$

In the odd-mode excitation, the intermediate node of TL can be regarded as virtual ground, so that TL with an electrical length $\theta_0/2$ is connected to P1′ and P3′, as illustrated in Fig. 4(b). Thus, the corresponding $[S]$ matrix of the coupler in the odd mode is

$$\begin{bmatrix} b_1 \\ b_2 \\ b_3 \\ b_4 \end{bmatrix} = [S_o] \begin{bmatrix} a_1 \\ a_2 \\ a_3 \\ a_4 \end{bmatrix} \tag{12}$$

in which

$$\Gamma_o = \frac{1 - j\tan(\theta_0/2)}{1 + j\tan(\theta_0/2)} \tag{13}$$

$$a_1 = \Gamma_o b_1 \tag{14}$$

$$a_3 = \Gamma_o b_3. \tag{15}$$

Then, from (12)–(15), the odd-mode $[S]$ matrix can be derived as follows:

$$\begin{bmatrix} b_2 \\ b_4 \end{bmatrix} = \begin{bmatrix} S_{22,o} & S_{24,o} \\ S_{24,o} & S_{44,o} \end{bmatrix} \times \begin{bmatrix} a_2 \\ a_4 \end{bmatrix} \tag{16}$$

where

$$S_{22,o} = S_{44,o} = \frac{\left(1 - k^2 - k^2(\sin\theta)^2\right)(j\tan(\theta_0/2) - 1)}{\Phi^2(j\tan(\theta_0/2) + 1)} \tag{17}$$

$$S_{24,o} = S_{42,o} = \frac{\left(jk\sqrt{1-k^2}\sin\theta\right)(j\tan(\theta_0/2) - 1)}{\Phi^2(j\tan(\theta_0/2) - 1)}. \tag{18}$$

After the scattering parameters in the even/odd modes are derived, the scattering matrix, $[S_C]$, of the proposed MDL coupler can be obtained by using the following equations:

$$S_{11,C} = S_{22,C} = S_{33,C} = S_{44,C} = \frac{S_{22,e} + S_{22,o}}{2} \tag{19}$$

$$S_{12,C} = S_{21,C} = S_{34,C} = S_{43,C} = \frac{S_{22,e} - S_{22,o}}{2} \tag{20}$$

$$S_{13,C} = S_{31,C} = S_{24,C} = S_{42,C} = \frac{S_{42,e} - S_{42,o}}{2} \tag{21}$$

$$S_{14,C} = S_{41,C} = S_{23,C} = S_{32,C} = \frac{S_{42,e} + S_{42,o}}{2}. \tag{22}$$

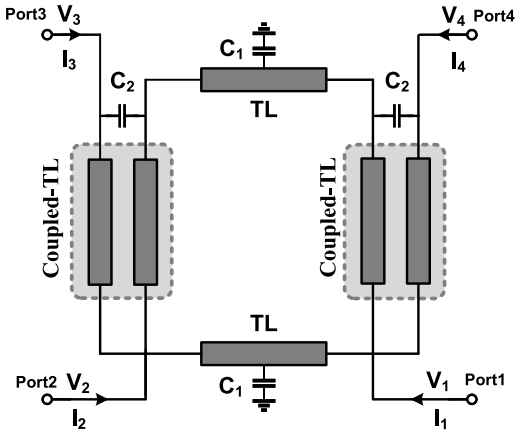

Fig. 5. Proposed coupler with the coupling capacitor C_2.

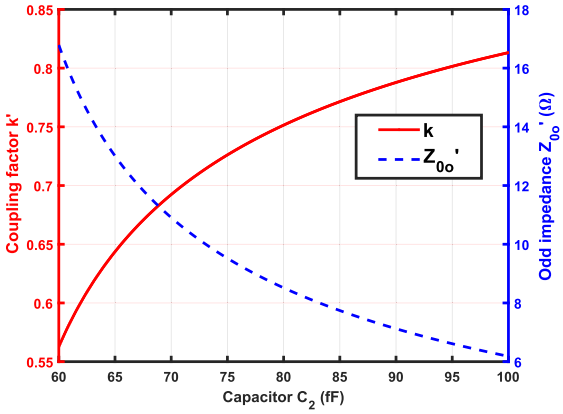

Fig. 6. Odd impedance Z_{0o} and coupler factor k' versus the coupling capacitor C_2 at 26 GHz.

By introducing (10), (11), (17), and (18) into (19)–(22), $[S_C]$ can be obtained, as shown in (23), at the bpttom of the page. Next, to derive the condition for the proposed coupler with ideal matching and isolation, the following boundary conditions are established:

$$S_{11,C} = 0 \tag{24}$$

$$S_{41,C} = 0. \tag{25}$$

Then, using (19) and (22) to express $S_{11,C}$ and $S_{41,C}$, we obtain the general conditions for the proposed coupler

$$\frac{(2 - j\tan(\theta_0/2))(j\omega C_1 Z_{0e} - 1)}{(j\tan(\theta_0/2) - 1)(j\omega C_1 Z_{0e} + 2)} = 1 \tag{26}$$

$$\frac{S_{21}}{S_{31}} = -j\frac{1 - k^2(1 + \sin\theta^2)}{2k\sqrt{1 - k^2}\sin\theta}. \tag{27}$$

The relationship of Z_0, θ, θ_0, and k is defined in (26) and (27). By selecting proper design parameters in (26), the desired matching and isolation for the coupler can be obtained. From (27), we can find there is a 90° phase difference between S_{21} and S_{31}, and θ and k can be properly adjusted to achieve the required 3-dB coupler for effective load modulation in LMBA.

B. Coupler Design With Coupling Capacitor

In fact, the coupling factor of the coupled line is dependent on the spacing and width of the coupled line as well as the material characteristics. Layout rules of line spacing usually affect the performance of the required coupling factor. For instance, in the 0.12-μm GaN-HEMT process, the spacing of metal lines must be greater than 2 μm, which limits the coupler design. To resolve this issue, as shown in Fig. 5, we introduce an extra coupling capacitor C_2 to adjust the capacitive coupling of coupled line for coupling factor implementation [31]. The new even/odd impedance of coupled line with C_2 can be derived as follows [28]:

$$Z'_{0e} = Z_{0e} \tag{28}$$

$$Z'_{0o} = \frac{B}{\sqrt{A^2 - 1}} \tag{29}$$

$$A = \cos\theta - \omega C_2 Z_{0o}\sin\theta \tag{30}$$

$$B = jZ_{0e}\sin\theta. \tag{31}$$

Thus, new coupling factor k' is given in (32), as shown at the bottom of the next page, by introducing new even/odd impedance into (2). From (32), we can find that the coupling factor of coupled lines is dependent on the value of C_2 when the electrical length θ and original even/odd impedance Z_{0e}/Z_{0o} are determined. Fig. 6 illustrates the odd-mode impedance Z'_{0o} and coupler factor k' versus the coupling capacitor C_2 at 26 GHz. As can be seen, the coupling factor k' increases from 0.55 to 0.82 as the capacitor C_2 arises from 60 to 100 fF, while the odd impedance Z'_{0o} decreases from 16.5 to 6 Ω. Therefore, the required coupling factor

$$[S_C] = \begin{bmatrix} \frac{(1-k^2-k^2\sin\theta^2)(\Gamma_e+\Gamma_o)}{2\Phi^2} & \frac{(1-k^2-k^2\sin\theta^2)(\Gamma_e-\Gamma_o)}{2\Phi^2} & \frac{\left(2k\sqrt{1-k^2}\sin\theta\right)(\Gamma_e-\Gamma_o)}{2\Phi^2} & \frac{\left(2k\sqrt{1-k^2}\sin\theta\right)(\Gamma_e+\Gamma_o)}{2\Phi^2} \\ \frac{(1-k^2-k^2\sin\theta^2)(\Gamma_e-\Gamma_o)}{2\Phi^2} & \frac{(1-k^2-k^2\sin\theta^2)(\Gamma_e+\Gamma_o)}{2\Phi^2} & \frac{\left(2k\sqrt{1-k^2}\sin\theta\right)(\Gamma_e+\Gamma_o)}{2\Phi^2} & \frac{\left(2k\sqrt{1-k^2}\sin\theta\right)(\Gamma_e-\Gamma_o)}{2\Phi^2} \\ \frac{\left(2k\sqrt{1-k^2}\sin\theta\right)(\Gamma_e-\Gamma_o)}{2\Phi^2} & \frac{\left(2k\sqrt{1-k^2}\sin\theta\right)(\Gamma_e+\Gamma_o)}{2\Phi^2} & \frac{(1-k^2-k^2\sin\theta^2)(\Gamma_e+\Gamma_o)}{2\Phi^2} & \frac{(1-k^2-k^2\sin\theta^2)(\Gamma_e-\Gamma_o)}{2\Phi^2} \\ \frac{\left(2k\sqrt{1-k^2}\sin\theta\right)(\Gamma_e+\Gamma_o)}{2\Phi^2} & \frac{\left(2k\sqrt{1-k^2}\sin\theta\right)(\Gamma_e-\Gamma_o)}{2\Phi^2} & \frac{(1-k^2-k^2\sin\theta^2)(\Gamma_e-\Gamma_o)}{2\Phi^2} & \frac{(1-k^2-k^2\sin\theta^2)(\Gamma_e+\Gamma_o)}{2\Phi^2} \end{bmatrix} \tag{23}$$

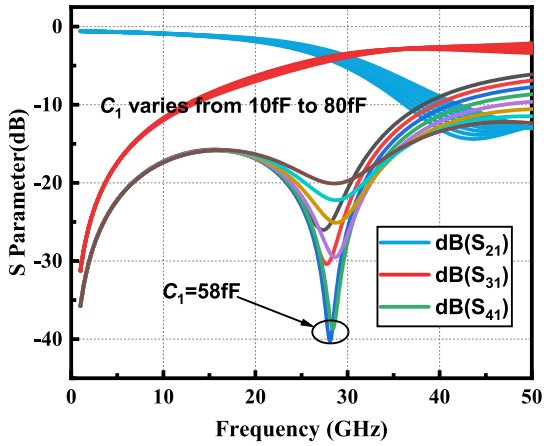

Fig. 7. Simulated S-parameter of the designed MDL coupler with different values of C_1.

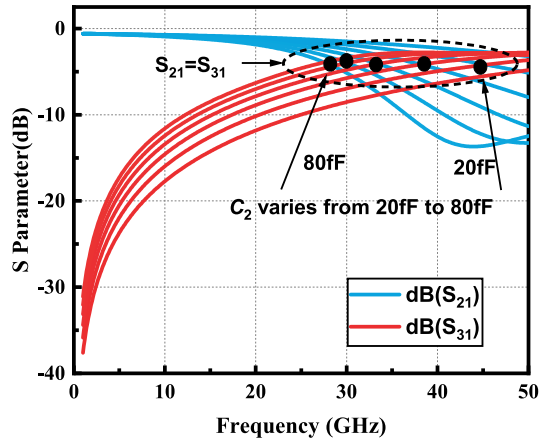

Fig. 8. Simulated S-parameter of the designed MDL coupler with different values of C_2.

can be achieved with the assistance of the coupling capacitor C_2, and thus, different electrical lengths θ can be used in the proposed MDL coupler to achieve the ideal coupler operation in different processes.

To better understand the proposed MDL coupler, the impact of the capacitors C_1 and C_2 is further investigated. From (26) and (27), we can see that the isolation of the coupler is dependent on C_1, while from (32), we can find that the directivity of the coupler can be adjusted by varying C_2. Figs. 7 and 8 show the simulation results. As can be seen, C_1 can effectively adjust the isolation of the designed coupler at different frequencies, and different values of C_2 can be used to change the frequency response of the coupler, S_{21} and S_{31}. Therefore, in practical implementation, C_1 and C_2 can be adjusted to achieve desired coupler operation when TL parameters, θ, Z_{0e}, Z_{0o}, and θ_0, are determined.

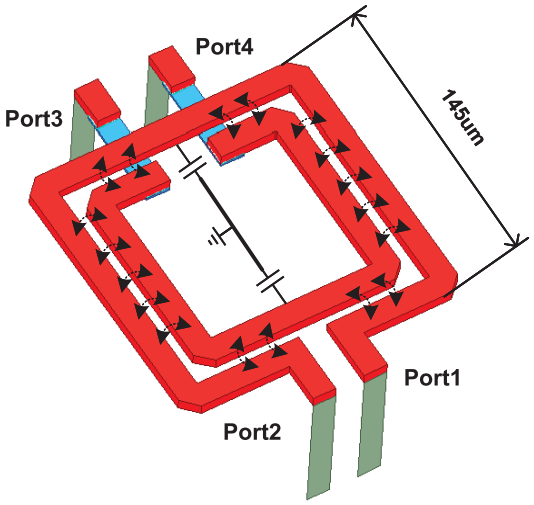

Fig. 9. Three-dimensional EM model of the designed MDL coupler.

Different from the traditional coupler where the electrical length θ of coupled lines must be designed to be $\lambda/4$ wavelength, in the proposed MDL coupler, the coupled line can be flexibly designed with any electrical length while using the corresponding capacitors C_1 and C_2 to achieve the required coupler performance from (27) and (32), which expands the design space of the coupler. For example, when all the TLs are determined, including the coupled TL with θ and Z_{0e}/Z_{0o}, and TL with θ_0 and Z_0, the capacitor C_1 and the coupling factor k can be calculated from (26) and (27). With (26) satisfied by the proper value of C_1, the currents generated by the magnetic coupling and electrical coupling will be canceled at the isolated port, where the isolation of the coupler will be infinite. Then, the coupling factor can be adjusted by the coupling capacitor C_2 from (32), accomplishing the required directivity of the coupler. The 3-D EM simulation model of the designed dual-loop coupler is presented in Fig. 9, which shows that the designed coupler only occupies 145 × 145 μm^2 core area excluding capacitors. With a C_1 of 20 fF, a C_2 of 37 fF, and a θ of 12°, the designed 3-dB MDL coupler presents a good performance with an isolation of −25 dB, a magnitude error of 0.14 dB, and a phase error of 1.5° at 26 GHz.

III. Design of RF-Input LMBA Using the Proposed MDL Coupler

Different from the traditional DPA, LMBA can modulate the impedance seen from the BA by injecting the control signal into the isolated port of the coupler, as shown in Fig. 10. The CA and BA branches are connected to input ports (Ports 2 and 3) and isolated port (Port 4) of the proposed MDL coupler, respectively. As discussed in Section II, there is a 90° phase offset between the current sources of Ports 2 and 3, while the CA signal at Port 4 can be assumed with a phase offset of φ

$$k' = \frac{Z_{0e}\sqrt{\left(1-\omega^2 C_2{}^2 Z_{0o}{}^2\right)\sin\theta^2 - \omega C_2 Z_{0o}\sin\theta + 2\cos\theta} - jZ_{0o}\sin\theta}{Z_{0e}\sqrt{\left(1-\omega^2 C_2{}^2 Z_{0o}{}^2\right)\sin\theta^2 - \omega C_2 Z_{0o}\sin\theta + 2\cos\theta} + jZ_{0o}\sin\theta} \tag{32}$$

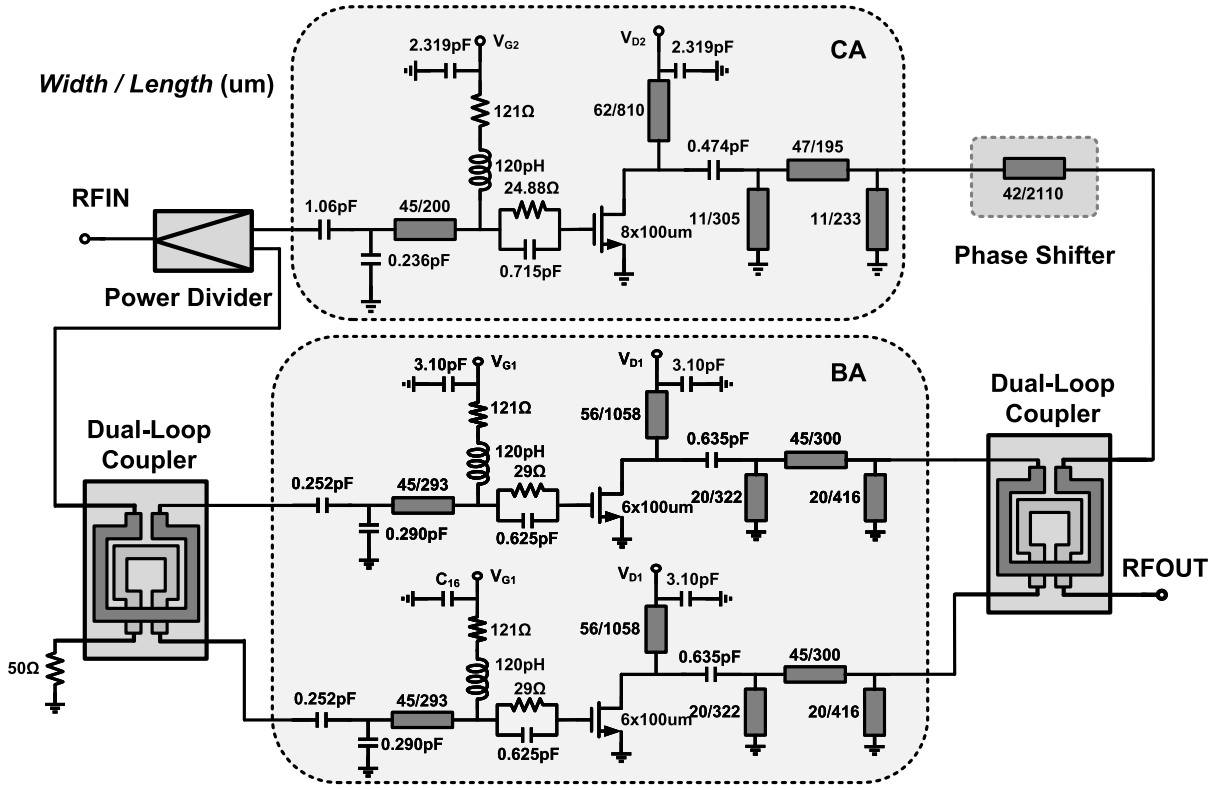

Fig. 10. Circuit schematic of the implemented LMBA.

from Port 2. The output port (Port 1) is terminated to the load with Z_0. Assuming that the designed MDL coupler is with a characteristic impedance Z_0 and all ports are matched, then the impedance of BA seen from the couple can be given by the following equation [14]:

$$Z_b = Z_0\left(1 + \frac{I_c e^{j\varphi}}{I_b}\right) \tag{33}$$

where Z_b is the impedance of BA branches seen from the coupler, and I_b and I_c are the current magnitude of BA and CA.

As illustrated in [21], when power arises to the desired PBO level, CA is turned on, and the impedance of BA is modulated to increase the power of BA. Then, the BA arrives in saturation at the first peak, which results in the output voltage of BA keeping constant after the desired PBO level. So, the following equation can be given:

$$Z_b i_{b,\text{peak1}} = \left(1 + \frac{\sqrt{2} i_{c,\text{peak2}}}{i_{b,\text{peak2}}}\right) Z_b \times i_{b,\text{peak2}} \tag{34}$$

where $i_{b,\text{peak1}}$, $i_{b,\text{peak2}}$, and $i_{c,\text{peak2}}$ are the peak current in the first and second efficiency peak points, respectively. The power of BA and CA can be calculated as follows:

$$P_{\text{BA}} = \begin{cases} 2i_b^2 Z_b, & i_c = 0 \\ \dfrac{2i_{b,\text{peak1}}^2 \times Z_b}{1 + \frac{\sqrt{2} i_c}{i_b}}, & i_c > 0 \end{cases} \tag{35}$$

$$P_{\text{CA}} = \begin{cases} 0, & i_c = 0 \\ i_c^2 Z_c, & i_c > 0 \end{cases} \tag{36}$$

where P_{BA} and P_{CA} represent the output power of BA and CA. Then, the output power transmitted to the load can be given as follows:

$$P_L = \begin{cases} 2i_b^2 Z_b, & i_c = 0 \\ i_c^2 Z_c + 2i_{b,\text{peak1}}^2 Z_b \dfrac{1}{1 + \frac{\sqrt{2} i_c}{i_b}}, & i_c > 0. \end{cases} \tag{37}$$

Therefore, the output OBO can be derived as follows:

$$\text{OBO} = \frac{P_{L,\text{peak1}}}{P_{L,\text{peak2}}} = \frac{1}{2}\left(\frac{\xi + \sqrt{2}}{1 + \sqrt{2}\xi}\right)^2 \tag{38}$$

where ξ represents the ratio of CA and BA current at the second peak efficiency point, i.e., $\xi = i_{c,\text{peak2}}/i_{b,\text{peak2}}$. According to (38), we can get the design relationship between OBO and ξ. For example, if the OBO level of 6 dB is required, ξ should be designed to be $-3\sqrt{2}/4$, which means the magnitude of CA current should be $3\sqrt{2}/4$ times as large as BA, and the phase offset between their currents should be 180°.

In this design, we aim to design a 4-W LMBA with 6-dB PBO capability. In order to achieve this, the power cell is designed to attain over 31-dBm output power considering the loss of passive components. Because of the high output power characteristics of GaN technology, a GaN-HEMT device with 100-μm width, 120-nm length, and six fingers is selected as a transistor cell to generate watt-level output power. To realize the targeted output power, the transistors are supplied with 28-V drain voltage, −1.6-V gate voltage of BA, and −3.6-V gate voltage of CA, respectively.

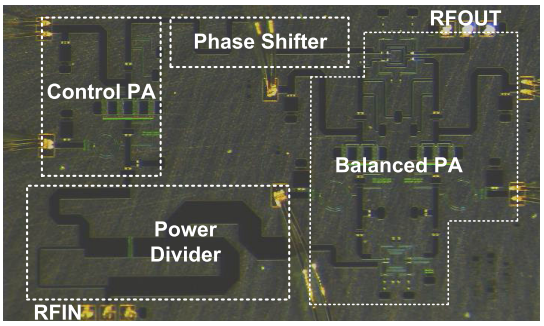

Fig. 11. Die microphotograph of the implemented LMBA.

As discussed above, the value of parameter ξ should be $-3\sqrt{2}/4$ for 6-dB PBO efficiency enhancement, which means the uneven power divider and phase shifter are needed to adjust the phase/magnitude relationship between CA and BA. In order to make good gain flatness, the codesign methodology between power units and power divider is needed. For input matching, a multiturn inductor is used as the bias network, and an RC network is inserted to improve the stability of the power cell. As for output matching, load–pull simulation is utilized to find the optimized impedance point from equal-efficient circle and equal-power circle. The schematic of the proposed LMBA and design parameters is shown in Fig. 10.

IV. Measurement Results

To fully verify the design, a 26-GHz LMBA using the proposed MDL couplers was fabricated in a 0.12-μm GaN-HEMT process with an area of 2.1 $\times$ 3.4 mm^2. The photomicrograph is shown in Fig. 11, where we can see that the fabricated coupler only occupies a footprint of 265 $\times$ 240 μm^2. The drains of transistors are biased at 28 V, while their gate biases are chosen as -1.6 and -3.6 V, respectively, to achieve high back-off efficiency enhancement. The chip die was wire-bonded to the test PCB, and onboard capacitors were used to filter the source noise and improve the stability of the system.

A. Small-Signal Measurement

The designed LMBA was tested under a small-signal condition first to validate the functionality of the circuit. A vector network analyzer from Keysight, E8361A, was used for S-parameter measurements. The on-wafer calibration was made by using a conventional short–load–open–thru (SLOT) to move the reference planes from the connectors of the equipment to the tips of the RF probes. For comparison, both the post-simulated and measured small-signal gain S_{21} and reflection responses S_{11} and S_{22} of the LMBA are plotted in Fig. 12. As illustrated, the discrepancy between the simulated and measured results is marginal. At 26 GHz, under a bias voltage of -3.6 V for the CA and -1.6 V for the BA, the measured small-signal gain is 7.01 dB. In addition, as expected, excellent impedance matching is obtained because of the use of the proposed MDL coupler.

B. Large-Signal Measurement

The performance of the designed LMBA was further evaluated with a continuous-wave (CW) large signal. The SMW00A

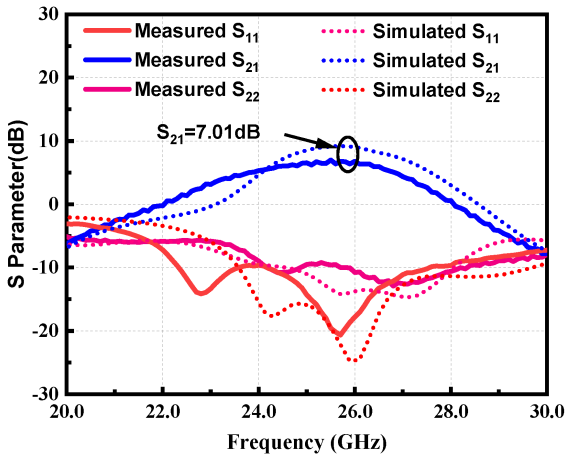

Fig. 12. Measured and simulated S-parameters of the designed LMBA.

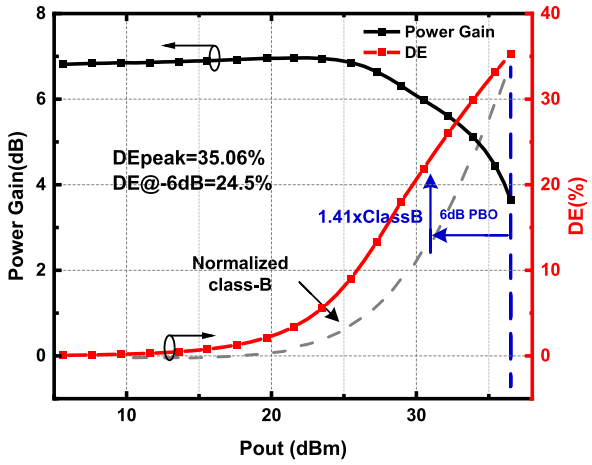

Fig. 13. Measured DE and power gain versus the output power at 26 GHz.

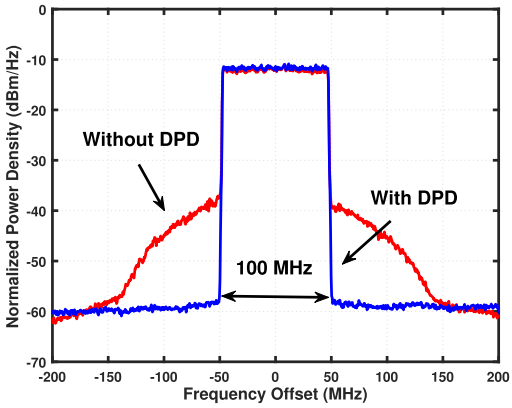

Fig. 14. Measured output spectrum for a 5G NR 100-MHz 64-QAM signal with/without DPD.

PSG Signal Generator from Rohde & Schwarz was used along with a highly linear driver amplifier to generate a CW input signal with sufficient power. The NRP50S USB Thermocouple Power Sensor with a 20-dB attenuator was used to measure the output power of the designed LMBA. The cable and connector losses were carefully characterized first and then de-embedded from the measured data. The measured gain and DE versus output power at 26 GHz is shown in Fig. 13. As can be seen, the DE of 35.06%/24.5% is obtained at peak power/6-dB

TABLE I
PERFORMANCE COMPARISON OF OTHER STATE-OF-THE-ART EFFICIENCY-ENHANCED PAS

Parameter	Doherty				LMBA			This work
	[33]JSSC'22	[34]TMTT'14	[35]TMTT'22	[36]TMTT'23	[37]JSSC'21	[38]TCASI'23	[39]TMTT'23	
Process	40 nm CMOS	0.15 μm GaAs pHEMT	0.15 μm GaN HEMT	0.15 μm GaN HEMT	28 nm CMOS	45 nm CMOS SOI	65 nm CMOS	0.12 μm HEMT GaN
Freq. (GHz)	29.5	24	26	28.5	36	40	27	26
Supply (V)	1	6	20	20	1	2	2	28
Gain (dB)	N/A	12.5	19.2*	20	18	16.8	24.8	7.01
P_{sat} (dBm)	18.7	30.9	35.1*	34.2	22.6	25.1	22.2	37.6
$PAE_{peak}(\%)$	24	38	35.8*	22	32	27.9	30.4	21.3
$PAE_{6dB}(\%)$	11.7	20	28.6*	15	24.2	19	16.5*	17.1
$DE_{peak}(\%)$	36	43.1*	40.1*	24.4*	33.7*	29.3	30.6*	35.06
$DE_{6dB}(\%)$	24.7	21.2*	30.2*	15.2*	24.6*	19.4	16.5*	24.5
Modulation	64-QAM	256-QAM	256-QAM	64-QAM	64-QAM	64-QAM	64-QAM	64-QAM
EVM (dB)	-27.58	N/A	-32.5#	-26.0	-25.1	-23.9	-25.9	-33.2#
P_{avg} (dBm)	7.9	23.5#	28	15	15.5	16.5	13.2	28#
ACLR (dBc)	-27.5	-36.2*#	-42.4#	-32	N/A	-25.3	-26.3	-47.61#

*Value extrapolated from graphs. #Measured results with DPD.

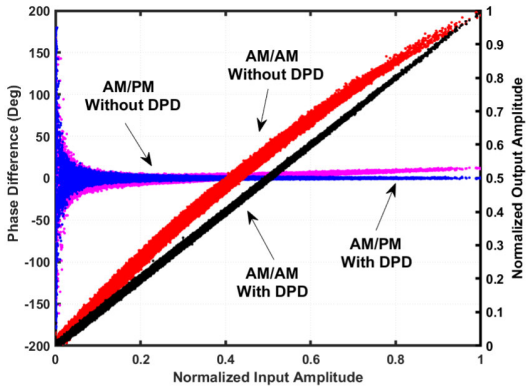

Fig. 15. Measured AM/AM and AM/PM at 28-dBm average output power using a 5G NR 100-MHz 64-QAM signal with 100-MHz BW.

back-off. The fabricated LMBA provides over 36-dBm output power and 1.41 times DE enhancement over an ideal Class-B PA at 6-dB PBO level.

C. Modulated Signal Measurement

The PA operation was also evaluated using a 5G NR FR2 64-QAM signal with up to 100-MHz modulation BW and 10.2-dB PAPR. The modulated signal was generated using a MATLAB code, loaded into an R&S SMW200A vector signal generator, and applied to the PA. The output signal was captured using an R&S FSW45 vector signal analyzer and was processed in MATLAB to extract the output signal features. The measured signal spectrum is shown in Fig. 14, where the ACLR, for BM = 100 MHz, is −34.1 dBc at lower/upper channels without DPD and improved to −47.1 dBc after DPD was applied [32]. The AM/AM and AM/PM characteristics with and without DPD for the 100-MHz signal are also given in Fig. 15. It can be seen that the designed LMBA with the proposed MDL coupler shows excellent linearity after the DPD is performed.

Table I compares the proposed design with the state-of-the-art PAs. Compared with other reported designs, the proposed LMBA achieves competitive efficiency enhancement at both P_{sat} and 6-dB PBO levels, despite using a miniaturized coupler with a minimal area of 265 × 240 μm^2 in GaN MMIC.

V. CONCLUSION

In this article, we presented a 26-GHz single-input LMBA using the proposed MDL coupler for back-off efficiency enhancement. The theoretical analysis and implementation details were fully described. Using the proposed MDL coupler, a single-input LMBA prototype was implemented in a standard 0.12-μm GaN-HEMT process. The designed LMBA achieved more than 36-dBm saturated output power with 1.41 times DE enhancement at 6-dB PBO level in comparison with the Class-B PA. More importantly, the design MDL coupler occupies an very small size of 265 × 240 μm^2, which can be an interesting candidate for compact ON-chip coupler implementation in the mm-wave band.

REFERENCES

[1] S. Hu, F. Wang, and H. Wang, "A 28-/37-/39-GHz linear Doherty power amplifier in silicon for 5G applications," *IEEE J. Solid-State Circuits*, vol. 54, no. 6, pp. 1586–1599, Jun. 2019.

[2] H. T. Nguyen and H. Wang, "A coupler-based differential mm-wave Doherty power amplifier with impedance inverting and scaling baluns," *IEEE J. Solid-State Circuits*, vol. 55, no. 5, pp. 1212–1223, May 2020.

[3] F. Wang and H. Wang, "A high-power broadband multi-primary DAT-based Doherty power amplifier for mm-wave 5G applications," *IEEE J. Solid-State Circuits*, vol. 56, no. 6, pp. 1668–1681, Jun. 2021.

[4] Z. Ma, K. Ma, K. Wang, and F. Meng, "A 28 GHz compact 3-way transformer-based parallel-series Doherty power amplifier with 20.4%/14.2% PAE at 6-/12-dB power back-off and 25.5 dBm PSAT in 55nm bulk CMOS," in *Proc. IEEE Int. Solid- State Circuits Conf. (ISSCC)*, vol. 65, Feb. 2022, pp. 320–322.

[5] X. Zhang, S. Li, D. Huang, and T. Chi, "A millimeter-wave three-way Doherty power amplifier for 5G NR OFDM," *IEEE J. Solid-State Circuits*, vol. 58, no. 5, pp. 1256–1270, May 2023.

[6] X. Li et al., "A 110-to-130 GHz SiGe BiCMOS Doherty power amplifier with a slotline-based power combiner," *IEEE J. Solid-State Circuits*, vol. 57, no. 12, pp. 3567–3581, Dec. 2022.

[7] F. Wang, T.-W. Li, S. Hu, and H. Wang, "A super-resolution mixed-signal Doherty power amplifier for simultaneous linearity and efficiency enhancement," *IEEE J. Solid-State Circuits*, vol. 54, no. 12, pp. 3421–3436, Dec. 2019.

[8] H.-C. Park et al., "Single transformer-based compact Doherty power amplifiers for 5G RF phased-array ICs," *IEEE J. Solid-State Circuits*, vol. 57, no. 5, pp. 1267–1279, May 2022.

[9] J. Pang, S. He, C. Huang, Z. Dai, J. Peng, and F. You, "A post-matching Doherty power amplifier employing low-order impedance inverters for broadband applications," *IEEE Trans. Microw. Theory Techn.*, vol. 63, no. 12, pp. 4061–4071, Dec. 2015.

[10] T.-Y. Huang, N. S. Mannem, S. Li, D. Jung, M.-Y. Huang, and H. Wang, "A 26-to-60 GHz continuous coupler-Doherty linear power amplifier for over-an-octave back-off efficiency enhancement," in *Proc. IEEE Int. Solid-State Circuits Conf. (ISSCC)*, vol. 64, Feb. 2021, pp. 354–356.

[11] E. Kaymaksut, D. Zhao, and P. Reynaert, "Transformer-based Doherty power amplifiers for mm-wave applications in 40-nm CMOS," *IEEE Trans. Microw. Theory Techn.*, vol. 63, no. 4, pp. 1186–1192, Apr. 2015.

[12] D. P. Nguyen, J. Curtis, and A.-V. Pham, "A Doherty amplifier with modified load modulation scheme based on load–pull data," *IEEE Trans. Microw. Theory Techn.*, vol. 66, no. 1, pp. 227–236, Jan. 2018.

[13] M. Bao, D. Gustafsson, R. Hou, Z. Ouarch, C. Chang, and K. Andersson, "A 24–28-GHz Doherty power amplifier with 4-W output power and 32% PAE at 6-dB OPBO in 150-nm GaN technology," *IEEE Microw. Wireless Compon. Lett.*, vol. 31, no. 6, pp. 752–755, Jun. 2021.

[14] D. J. Shepphard, J. Powell, and S. C. Cripps, "An efficient broadband reconfigurable power amplifier using active load modulation," *IEEE Microw. Wireless Compon. Lett.*, vol. 26, no. 6, pp. 443–445, Jun. 2016.

[15] R. Quaglia and S. Cripps, "A load modulated balanced amplifier for telecom applications," *IEEE Trans. Microw. Theory Techn.*, vol. 66, no. 3, pp. 1328–1338, Mar. 2018.

[16] Y. Cao, H. Lyu, and K. Chen, "Asymmetrical load modulated balanced amplifier with continuum of modulation ratio and dual-octave bandwidth," *IEEE Trans. Microw. Theory Techn.*, vol. 69, no. 1, pp. 682–696, Jan. 2021.

[17] P. H. Pednekar, E. Berry, and T. W. Barton, "RF-input load modulated balanced amplifier with octave bandwidth," *IEEE Trans. Microw. Theory Techn.*, vol. 65, no. 12, pp. 5181–5191, Dec. 2017.

[18] P. H. Pednekar, W. Hallberg, C. Fager, and T. W. Barton, "Analysis and design of a Doherty-like RF-input load modulated balanced amplifier," *IEEE Trans. Microw. Theory Techn.*, vol. 66, no. 12, pp. 5322–5335, Dec. 2018.

[19] C. Chu et al., "Waveform engineered sequential load modulated balanced amplifier with continuous class-F-1 and class-J operation," *IEEE Trans. Microw. Theory Techn.*, vol. 70, no. 2, pp. 1269–1283, Feb. 2022.

[20] J. Pang et al., "Analysis and design of highly efficient wide-band RF-input sequential load modulated balanced power amplifier," *IEEE Trans. Microw. Theory Techn.*, vol. 68, no. 5, pp. 1741–1753, May 2020.

[21] J. Pang, C. Chu, Y. Li, and A. Zhu, "Broadband RF-input continuous-mode load-modulated balanced power amplifier with input phase adjustment," *IEEE Trans. Microw. Theory Techn.*, vol. 68, no. 10, pp. 4466–4478, Oct. 2020.

[22] Y. Cao, H. Lyu, and K. Chen, "Load modulated balanced amplifier with reconfigurable phase control for extended dynamic range," in *IEEE MTT-S Int. Microw. Symp. Dig.*, Jun. 2019, pp. 1335–1338.

[23] T.-Y. Huang, N. S. Mannem, S. Li, D. Jung, M.-Y. Huang, and H. Wang, "A coupler balun load-modulated power amplifier with extremely wide bandwidth," *IEEE Trans. Microw. Theory Techn.*, vol. 71, no. 4, pp. 1573–1586, Apr. 2023.

[24] J. R. Powell, D. J. Shepphard, R. Quaglia, and S. C. Cripps, "A power reconfigurable high-efficiency X-band power amplifier MMIC using the load modulated balanced amplifier technique," *IEEE Microw. Wireless Compon. Lett.*, vol. 28, no. 6, pp. 527–529, Jun. 2018.

[25] Q. Xu and Y. Ethan Wang, "Design and realization of compact folded Lange coupler," in *IEEE MTT-S Int. Microw. Symp. Dig.*, Jun. 2012, pp. 1–3.

[26] A. Bikiny et al., "Ka-band Lange coupler in multilayer thick-film technology," in *IEEE MTT-S Int. Microw. Symp. Dig.*, Jun. 2009, pp. 1001–1004.

[27] L. Chen, H. Liu, J. Hora, J. A. Zhang, K. S. Yeo, and Z. Xi, "A monolithically integrated single-input load-modulated balanced amplifier with enhanced efficiency at power back-off," *IEEE J. Solid-State Circuits*, vol. 56, no. 5, pp. 1553–1564, May 2021.

[28] D. M. Pozar, *Microwave Engineering*, 4th ed. Hoboken, NJ, USA: Wiley, 2011.

[29] F. Wang and H. Wang, "A broadband linear ultra-compact mm-wave power amplifier with distributed-balun output network: Analysis and design," *IEEE J. Solid-State Circuits*, vol. 56, no. 8, pp. 2308–2323, Aug. 2021.

[30] H. Jia, B. Chi, L. Kuang, and Z. Wang, "A W-band power amplifier utilizing a miniaturized Marchand balun combiner," *IEEE Trans. Microw. Theory Techn.*, vol. 63, no. 2, pp. 719–725, Feb. 2015.

[31] C. Caloz and T. Itoh, "A novel mixed conventional microstrip and composite right/left-handed backward-wave directional coupler with broadband and tight coupling characteristics," *IEEE Microw. Wireless Compon. Lett.*, vol. 14, no. 1, pp. 31–33, Jan. 2004.

[32] A. Zhu, "Decomposed vector rotation-based behavioral modeling for digital predistortion of RF power amplifiers," *IEEE Trans. Microw. Theory Techn.*, vol. 63, no. 2, pp. 737–744, Feb. 2015.

[33] M. Mortazavi, Y. Shen, D. Mul, L. C. N. de Vreede, M. Spirito, and M. Babaie, "A four-way series Doherty digital polar transmitter at mm-Wave frequencies," *IEEE J. Solid-State Circuits*, vol. 57, no. 3, pp. 803–817, Mar. 2022.

[34] R. Quaglia, V. Camarchia, T. Jiang, M. Pirola, S. D. Guerrieri, and B. Loran, "K-band GaAs MMIC Doherty power amplifier for microwave radio with optimized driver," *IEEE Trans. Microw. Theory Techn.*, vol. 62, no. 11, pp. 2518–2525, Nov. 2014.

[35] R.-J. Liu et al., "A 24–28-GHz GaN MMIC synchronous Doherty power amplifier with enhanced load modulation for 5G mm-wave applications," *IEEE Trans. Microw. Theory Techn.*, vol. 70, no. 8, pp. 3910–3922, Aug. 2022.

[36] A. Piacibello, V. Camarchia, P. Colantonio, and R. Giofrè, "3-way Doherty power amplifiers: Design guidelines and MMIC implementation at 28 GHz," *IEEE Trans. Microw. Theory Techn.*, vol. 71, no. 5, pp. 2016–2028, May 2023.

[37] V. Qunaj and P. Reynaert, "A Ka-band Doherty-like LMBA for high-speed wireless communication in 28-nm CMOS," *IEEE J. Solid-State Circuits*, vol. 56, no. 12, pp. 3694–3703, Dec. 2021.

[38] L. Chen, L. Chen, Z. Ge, Y. Sun, and X. Zhu, "A 40-GHz load modulated balanced power amplifier using unequal power splitter and phase compensation network in 45-nm SOI CMOS," *IEEE Trans. Circuits Syst. I, Reg. Papers*, vol. 70, no. 8, pp. 3178–3186, Jun. 2023.

[39] C. Zhao et al., "A Ka-band pseudo-Doherty load-modulated balanced amplifier with gain flatness enhancement technique," *IEEE Trans. Microw. Theory Techn.*, vol. 72, no. 6, pp. 3423–3437, Jun. 2024.

Haoyang Jia (Graduate Student Member, IEEE) received the B.E. and M.E. degrees from South China University of Technology (SCUT), Guangzhou, China, in 2019 and 2022, respectively. He is currently pursuing the Ph.D. degree at the University College Dublin (UCD), Dublin, Ireland.

He is with the RF and Microwave Research Group, University College Dublin. His current research interests include integrated high-efficiency power amplifier (PA) design, and next-generation transmitter and receiver design.

Ruijia Liu (Member, IEEE) received the B.E. degree in electronic information science and technology from Southwest Jiaotong University (SWJTU), Chengdu, China, in 2017, and the Ph.D. degree in electromagnetic field and microwave technology from Southeast University (SEU), Nanjing, China, in 2022.

Since October 2022, he has been a Post-Doctoral Research Fellow with the RF and Microwave Research Group, University College Dublin (UCD), Dublin, Ireland. His current research interests include broadband high-efficiency gallium nitride (GaN) power amplifier (PA) design and GaN monolithic microwave-integrated circuit PA design for RF/microwave and millimeter-wave applications.

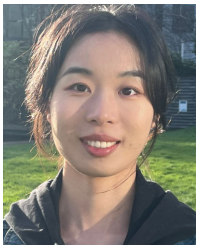

Qian Wu (Graduate Student Member, IEEE) received the B.E. degree from Nanjing University of Posts and Telecommunications, Nanjing, China, in 2019, and the M.E. degree from Southeast University, Nanjing, in 2022. She is currently pursuing the Ph.D. degree at the RF and Microwave Research Group, University College Dublin (UCD), Dublin, Ireland.

Her research interests include linearization techniques for power amplifiers and beamforming systems.

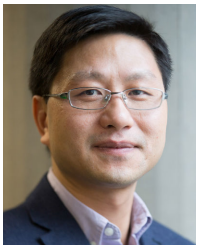

Anding Zhu (Fellow, IEEE) received the Ph.D. degree in electronic engineering from the University College Dublin (UCD), Dublin, Ireland, in 2004.

He is currently a Professor with the School of Electrical and Electronic Engineering, UCD. His research interests include high-frequency nonlinear system modeling and device characterization techniques, high-efficiency power amplifier design, wireless transmitter architectures, digital signal processing, and nonlinear system identification algorithms.

Prof. Zhu is an Elected Member of the IEEE Microwave Theory and Technology Society (MTT-S) Administrative Committee (AdCom). He was a recipient of the 2021 IEEE MTT-S Microwave Prize. He is the Chair of the IEEE MTT-S Technical Coordination and Future Directions Committee. He served as the Secretary of the IEEE MTT-S AdCom in 2018 and the Chair of the IEEE MTT-S Microwave High-Power Techniques Committee (TC-12) in 2020 and 2021. He served as a Track Editor for IEEE TRANSACTIONS ON MICROWAVE THEORY AND TECHNIQUES from 2020 to 2022. He is an Associate Editor of *IEEE Microwave Magazine*.